Article:
Grecchi, E, O'Doherty, J, Veronese, M et al. (2015) Multimodal Partial-Volume Correction: Application to 18F-Fluoride PET/CT Bone Metastases Studies. Journal of Nuclear Medicine, 56 (9). pp. 1408-1414. ISSN: 0161-5505

https://doi.org/10.2967/jnumed.115.160598

Multimodal Partial Volume Correction – Application to ^{18}F-Fluoride PET-CT bone metastases studies

Elisabetta Grecchi[1,2], Jim O'Doherty[3], Mattia Veronese[1], Charalampos Tsoumpas[2,4], Gary J. Cook[2,3] and Federico E. Turkheimer[1]

[1]Centre for Neuroimaging, Institute of Psychiatry, Psychology and Neuroscience King's College London, London, UK

[2]Division of Imaging Sciences & Biomedical Engineering, King's College London, London, UK

[3]PET Imaging Centre, Division of Imaging Sciences & Biomedical Engineering, King's College London, King's Health Partners, St Thomas's Hospital, London, UK

[4]Division of Biomedical Imaging, University of Leeds, Leeds, UK

Running title multimodal PVC in ^{18}F-Fluoride bone PET

ABSTRACT

^{18}F-Fluoride PET-CT offers the opportunity for accurate skeletal metastasis staging compared to conventional imaging methods. ^{18}F-Fluoride is a bone specific tracer whose uptake depends on osteoblastic activity. The osteoblastic process can also be detected morphologically in CT images due to the resulting increase in bone mineralization and sclerosis. Whilst CT is characterized by high resolution, the potential of PET is limited by its lower spatial resolution and the resulting partial volume effect. In this context, the synergy between PET and CT presents an opportunity to resolve this limitation using a novel multimodal approach called Synergistic-Functional-Structural Resolution-Recovery (SFS-RR). Its performance is benchmarked against current resolution recovery technology employing the point-spread-function (PSF) of the scanner in the reconstruction procedure.

Methods - The SFS-RR technique takes advantage of the multiresolution property of the wavelet transform applied to both functional and structural images to create a high-resolution PET that exploits the structural information of CT. Although the method was originally conceived for PET-MRI brain data, an ad-hoc version for whole body PET-CT is here proposed.

Three phantom experiments and two datasets of metastatic bone ^{18}F-Fluoride PET-CT images from primary prostate and breast cancer were used to test the algorithm performances. The SFS-RR images were compared with the manufacturer's PSF based reconstruction using the standardized uptake value (SUV*)* and the metabolic volume as metrics for quantification.

Results – When compared to standard PET images the phantom experiments showed a bias reduction of 14% in activity and 1.3cm^3 in volume estimates for PSF images and up to 20% and 2.5cm^3 for the SFS-RR images. The SFS-RR images were characterized by a higher recovery coefficient (up to 60%) while noise levels remained comparable to those of standard PET.

The clinical data showed an increase in the SUV estimates for SFS-RR images up to 34% for SUV_{peak} and 50% for SUV_{max} and SUV_{mean}. Images were also characterized by sharper lesion contours and better lesion detectability.

Conclusion - The proposed methodology generates PET images with improved quantitative and qualitative properties. Compared to standard methods, SFS-RR provides superior lesion segmentation and quantification, which may result in more accurate tumor characterization.

Key Words ^{18}F-Fluoride, partial volume correction, PET/CT, wavelet, multimodal imaging

INTRODUCTION

Up to 70% of patients with prostate and breast cancer will develop bone metastases (*1, 2*). ^{18}F-Fluoride has shown efficacy in both diagnosis and treatment response assessment (*3-6*) and recent studies on skeletal metastases report improved diagnostic sensitivity and specificity when morphologic evaluation from computed tomography (CT) scans are combined with functional evaluation of ^{18}F-Fluoride positron emission tomography (PET) (*7, 8*). This radiotracer accumulates at skeletal metastatic sites as a result of increased blood flow, osteoblastic activity and bone mineralization (*9-11*). In prostate cancer, ^{18}F-Fluoride accumulation corresponds to sites of osteosclerosis and increased bone density that are usually visible on CT (*12*).

Evaluation criteria for tumor staging and response assessment include visual and/or quantitative evaluation of the extent, intensity and changes in ^{18}F-Fluoride uptake in bone lesions (*13*). In this perspective the influence of the partial volume effect (PVE) is of impact (*14*) when comparing activity and morphological changes pre- and post- therapy (*15, 16*) considering the poor image resolution and quantification bias resulting from activity spill-over. PVE in PET has been addressed with several imaged-based partial volume correction (PVC) methods (*17*) that can be classified as either voxel-based methods, such as partition-based (*18*), multiresolution (*19, 20*), or region of interest (ROI)-based techniques (*21, 22*), which are limited by assumptions of radiotracer distribution homogeneity in the area of interest. A distinct approach consists of the incorporation of a model for the system point-spread-function (PSF) within the image reconstruction algorithm to account for resolution degradation (*23, 24*).

In this study our aim was to correct for the PVE in whole-body ^{18}F-Fluoride PET-CT to allow a more robust lesion classification in terms of activity quantification and volume definition. The methodology was developed from previous work by Shidahara et al (*20*) and exploits the local functional/structural relationship of PET-CT in a synergistic fashion for a realistic noise controlled resolution recovery of PET images, hence the name Synergistic-Functional-Structural Resolution-Recovery (SFS-RR). Here the SFS-RR algorithm is optimized for ^{18}F-Fluoride PET given the correlation between functional (fluoride uptake) and morphological (sclerosis) signals on PET and CT images. For

benchmarking the resulting images were compared to standard reconstructed PET images and images reconstructed with the inclusion of the PSF model (*25*).

MATERIALS AND METHODS

Image Resolution Recovery

The Synergistic-Functional-Structural Resolution-Recovery (SFS-RR) algorithm was first introduced by Shidahara et al. (*20*) for partial volume correction of brain PET-MR data. The structural information was exploited by segmenting a T1-MRI image through a probability atlas (*26*) defining 83 anatomical regions. Hence, the resolution recovery is ROI-based and relies on good co-registration between PET and MRI images as well as between MRI and the probability atlas. The idea stems from previous concepts on wavelet-based resolution recovery (*19*) and de-noising (*27*).

In this work we developed SFS-RR further to fit a novel clinical requirement, specifically ^{18}F-Fluoride PET-CT for detecting and monitoring bone metastases. The choice of the application is not fortuitous; in the first instance, PET-CT images provide synergistic information (i.e. both modalities show high image intensity in correspondence of lesions) and, secondly, they do not require additional coregistration as for two separate PET and MR acquisitions. Furthermore all the structural information of interest is contained in the CT and can be automatically segmented for each subject with no need for a universal atlas. The algorithm decomposes both functional (PET) and anatomical (CT) images into several resolution elements by means of a wavelet transform. The high-resolution components of both modalities are then combined together via a statistical model with appropriate scaling, resolution correction and weighting, to create a high-resolution PET image that exploits the structural information, when present, but preserves PET data when matching structural data are not present.

Anatomical Image Segmentation

In their original work, Shidahara et al. (*20*) proposed the use of an anatomical brain atlas to obtain suitable anatomical images. In brain studies this is a reasonable procedure given the possibility of normalizing to a common space (e.g. probabilistic atlas).

In whole-body PET-CT, the atlas-based approach is not feasible. In ^{18}F-Fluoride PET-CT acquisitions the good spatial correlation between morphological and functional information is such that the CT images of each subject can be processed individually to highlight the structures of interest supplying the required structural base.

The first step consists of an initial coarse segmentation of the CT images based on thresholding the Hounsfield Units (HU) values as follow: bone ($100 \leq HU < 1400$), soft tissue ($0 \leq HU < 100$) and fat ($-150 \leq HU < 0$) (*28*).

Bone is further segmented into 100 bins after image histogram equalization. New intensity values are assigned to all the segmented regions. These intensity values are calculated from the average of each corresponding region in the original PET image to obtain the subject-specific structural reference image used as anatomical information for the SFS-RR algorithm (*20, 29*) (Supplementary Materials Figure 1).

Image segmentation and the SFS-RR algorithm implementation were both performed in Matlab R2011b (The Mathworks Inc., Natick MA, USA). The whole procedure is schematically described in Figure 1; for a more detailed mathematical exposition the reader is referred to the Supplementary Materials (Synergistic-Functional-Structural Resolution Recovery Algorithm section).

Phantom Data

For the evaluation of the SFS-RR method we used the NEMA IEC body phantom and an insert with six spheres of different volumes, 26.52 cm^3 (S1), 11.49 cm^3 (S2), 5.57 cm^3 (S3), 2.57 cm^3 (S4), 1.15 cm^3 (S5) and 0.52 cm^3 (S6), respectively. Compartments were filled with both iodinated contrast media (CM) Omnipaque300^{TM} (300 mg/ml organic Iodine) and radioactive tracer ^{18}F-Fluoride. We aimed to reproduce contrast levels between different structures in both the PET and CT images as observed in clinical ^{18}F-Fluoride bone scans. Specifically, we reproduced PET and CT contrasts as observed in normal soft tissue, normal bone and metastatic bone. We performed three different experiments changing the layout of CT and PET contrasts. This aimed to account for possible mismatches between functional and anatomical images (i.e. whereas a lesion would be detectable in only one imaging modality) resulting in a more robust method validation for

what concern the phantom experiments. A summary of CM and radiotracer concentrations used in each experiment is reported in Table 1. For a detailed description of the experimental procedure we refer to Grecchi et al. 2014 (*30*).

Images were acquired on a GE Discovery 710 PET-CT scanner (General Electric Medical System, Milwaukee, WI, USA). CT scans were performed with a routine clinical protocol (115 mA, 140 kVp and 0.5 second gantry rotation speed) followed by a fully 3D PET Time Of Flight (TOF) acquisition. PET data were reconstructed using our routine clinical protocol, a standard TOF Ordered Subsets Expectation Maximization (OSEM) algorithm (24 subsets, 2 iterations) (GE Q.Core VuePoint FX, henceforth called *Standard PET*). The resulting images were then processed with the SFS-RR algorithm. In addition we reconstructed the same data with the inclusion of a Point Spread Function (PSF) model into the standard TOF-OSEM algorithm (GE Q.Core VuePoint FX-S, henceforth called *PET-PSF*).

All the images were finally smoothed with a Gaussian 3D filter FWHM 6.4mm; this is required by PSF reconstructed images as well when used in clinical routine given that increased noise level hamper visual assessment.

Clinical Dataset

The impact of the proposed resolution recovery technique was tested with two different sets of oncological patient data, both characterized by the presence of bone metastases. The institutional review board approved this study and all subjects signed a written informed consent.

The first dataset was a prospective observational study of patients with bone-predominant metastatic prostate cancer, at first diagnosis or at progression of disease, who were embarking on docetaxel chemotherapy. The second data set was a prospective observational study of patients with bone-predominant metastatic breast cancer, at first diagnosis or at progression of disease, who were embarking on a new line of endocrine treatment in combination with bone-targeted therapy. In total 7 patients with active skeletal metastases were included in the analysis, 4 with prostate cancer and 3 with breast cancer.

In each patient a whole body ^{18}F-Fluoride PET-CT scan was acquired with a total of 8 bed positions, from the base of the skull to upper thighs, 60 minutes after injection of approximately 250MBq.

The image reconstruction protocol for both datasets was the same as for the phantom experiment, with the exclusion of the PSF reconstruction, which was not performed as it was not included in the clinical protocol.

Data Analysis

In-house software was used to perform quantitative analysis on both phantom and patient data. An ROI was manually drawn on the outer border of each lesion in order to completely contain the whole lesion volume (or sphere for the phantom data) and then automatically segmented with a threshold of 40% of the maximum value of the ROI. The SUV_{mean}, SUV_{max}, SUV_{peak} and lesion metabolic active tumor volume (MATV) were then computed for the automatically segmented ROI. SUV_{peak} is computed here as the mean SUV measured over a fixed small circular volume of about 1cm^3, in the hottest area of the tumor (more active region). It is considered more reproducible since it involves the mean value of a few voxels involving and surrounding the hottest tumor area.

Solely for the phantom experiments, knowing the ground truth, we used the Root Mean Square Error (RMSE) and Contrast to Noise Ratio (CNR) as additional metrics for image quality assessment. Specifically, we evaluated the quantification accuracy and the trade-off between contrast improvement and image noise. The two metrics are defined as follow

$$\mathrm{RMSE} = 100\times\sqrt{\frac{\left(\mathrm{A_S}-\mathrm{A_{S,true}}\right)^2}{\mathrm{A_{S,true}}^2}}$$

$$\mathrm{CNR} = \frac{\mathrm{A_S}-\mathrm{A_{back}}}{\sigma_{\mathrm{back}}}$$

A_S represents the mean activity estimated inside a sphere and $\mathrm{A_{S,true}}$ the corresponding ground truth while $\mathrm{A_{back}}$ is the mean activity estimated in the phantom background and σ_{ack} its standard deviation.

RESULTS

Phantom Data

Figure 2 shows representative transaxial views of structural (CT) and functional (PET) images for the three phantom experiments, one for each line. PET images from PSF reconstruction (PET-PSF) and from the application of the Resolution Recovery algorithm (PET-SFS) are also displayed. In Figure 2 Supplementary Material are reported as well representative line profiles for the three experiments for spheres 4-5.

Improved qualitative resolution for the smaller structures (red marker in Figure 2) is noted when the SFS-RR algorithm is applied. Even though larger spheres (green and blue markers in Figure 2) are easily detectable in the images from all modalities, it is possible to appreciate a reduction in the blurring surrounding the structure when the resolution recovery algorithm is implemented.

Furthermore it is possible to appreciate the robustness of the anatomy-based resolution recovery algorithm to unexpected mismatches between anatomy and functional acquisition by studying images from Experiment 1. Even though spheres 4-6 cannot be detected on the CT they are not lost in the new functional image returned by the SFS-RR algorithm.

The quantitative evaluation of functional images obtained with the three different methods is reported in Table 2. The table reports for each phantom compartment in all the experiments the estimates of SUV_{mean}, SUV_{max}, SUV_{peak} and MATV together with the corresponding ground-truth values.

A summary of methods performances is summarized in the supplementary materials (Figure 3) as the average among the three experiments. The general trend shows that the smaller the sphere, the bigger the bias in the activity estimation, regardless of the method used. However, with the SFS-RR application the bias decreases with an average range of 1-5% in the PET-PSF images and 5-19% in PET-SFS images. The same trend applies to lesion size estimation where the bias decreases in a range of 0.46-0.95 cm for PET-PSF data and 0.56-1.09 cm for PET-SFS data.

The better performances of the SFS-RR algorithm are upheld by the root mean square error (RMSE) and contrast to noise ratio (CNR) comparison in Figure 3. Images resulting from the application of the SFS algorithm show lower *RMSE* on average (up to 15% compared to standard PET for the smallest sphere) while being consistent with the trend of the RMSE increasing for smaller spheres. It is of note that the improved image resolution does not

come with a detriment of image quality as noise levels are contained with CNR either higher or comparable with the standard PET image.

Clinical Dataset

The influence of using the SFS-RR algorithm on real patient data can be appreciated qualitatively in Figure 4 (and Figures 4-6 in Supplementary Materials) where the Maximum Intensity Projection (MIP) and two different transaxial views are displayed for a representative subject.

There is a clear increase in lesion sharpness following the application of a resolution recovery technique. The quantitative characterization of all lesions of this specific subject is reported in the Supplementary Materials (Figure 7 and Table 1). The transaxial views of Figure 4 is a good example of the effect in lesion definition and characterization using the SFS-RR algorithm. Sharper contours and the activity recovery in the PET-SFS images for the rib lesion (Figure 4, transaxial view, red marker) and also in the spine (Figure 4, transaxial view, blue marker) are evident, and in the spine lesion it is easier to appreciate that the activity is in the periphery of the lesion where there is greatest osteoblastic activity compared to the relatively photopenic center. In terms of quantitative characterization there is an increase in the SUV_{mean} estimates of 60% (rib lesion, SUV_{PET}=30.7 SUV_{SFS}=49.1) and 43% (spine lesion, SUV_{PET}=23.2 SUV_{SFS}=33.1) from the standard-PET to the PET-SFS. In contrast, the automatic segmented MATV has a relative reduction of 25% (rib lesion, $MATV_{PET}$=2.7cm^3 $MATV_{SFS}$ =2.1cm^3) and 31% (spine lesion, $MATV_{PET}$=7.5cm^3 $MATV_{SFS}$=5.2cm^3).

A comprehensive comparison of the quantitative differences due to application of the SFS-RR algorithm is reported in Figure 5. As previously performed for Patient 01 (Figure 7 - Table 1 Supplementary Materials) we segmented all lesions of the remaining patients and collected the corresponding values of SUV_{mean}, SUV_{max}, SUV_{peak} and MATV. Figure 5 reports the relative differences (SUVs and MATV) between lesions segmented in standard PET and PET-SFS images for the entire datasets.

There is a general increment in activity estimates for PET-SFS compared to standard PET. The average increments for different indexes are as follow: ΔSUV_{mean} = 49%, ΔSUV_{max} =

47% and ΔSUV_{peak} = 34%. For low activity lesions the range of differences in the estimates is larger than for more active lesions indicating that the algorithm efficiency is dependent on signal to noise ratio. For the MATV there is an average reduction of 1.4cm^3 when segmentation is performed on PET-SFS images. When lesion size increases the difference reached values of 4-5cm^3, which might be relevant if patient classification were based on characterization of the larger detectable lesions.

DISCUSSION

In this work we evaluated the influence of a multimodal partial volume correction technique on the quantification and assessment of metastatic bone lesions from primary prostate and breast cancers. It is worth remarking that this work targets specifically to ^{18}F-Fluoride PET/CT bone scans as SFS-RR obviously produces better results the stronger is the correspondence between functional and structural signals. Our results showed an average 50% increase in SUV_{max} and SUV_{mean} and a 30% increase in the SUV_{peak} for partial-volume corrected images when compared with the standard PET, depending on lesion size (lesion volume range 0.5–25cm^3). Our results are in agreement with findings in similar experimental settings from previous studies (*31, 32*). Although SUV_{max} estimates depend on image noise, the 50% increase is not a consequence of noise bursts given the comparable RMSE between the SFS-RR corrected images and standard PET images.

The higher activity recovery and the good noise control from the phantom analysis indicate a better image quality when the SFS-RR algorithm is applied. Indeed patient images show lesions with sharper and better-defined contours, which result in improved lesion conspicuity and segmentation even for smaller volumes. To note that the CNR depends on the absolute activity value and that explains why on Figure 3 one set of spheres show higher CNR than the other.

The results from the phantom experiments showed that the SFS-RR images outperform both standard PET and PSF images in terms of image quality and quantification accuracy. PSF-based image reconstruction is known to contribute to the appearance of artefacts (*33*) and is computationally cumbersome hence is not performed in routine clinical studies in our Unit; for this reason standard PET was used as a reference for SFS-RR

images when it came to patients image analysis. In this regard, it is worth noting that no artefacts have been generally observed in this and previous applications of SFS-RR which is now a mature enough technology worth further testing in the clinical setting.

It is worth highlighting the robustness of the methodology regarding possible mismatch between PET and CT images. Phantom acquisitions showed that even if some structures are only visible on the functional images, they are preserved after the application of the algorithm. This is of importance because lesions that might be lost in the CT segmentation, for example because their size is too small or the metastasis does not show sufficient bone mineralization to appear sclerotic, they will still be visible in the final enhanced PET images.

Although the SFS-RR algorithm showed qualitatively and quantitatively better images than standard PET, further analyses are necessary to quantify the influence of the improved image quality on the assessment of patient skeletal staging and therapy response. This may allow better definition and quantification of lesions following therapy or allow greater detectability and segmentation of metastatic spread at staging. Of interest would be also to evaluate whether lesion heterogeneity is affected by higher resolution and evaluate the consequent impact on textural analysis, given its increasing oncological applications (*34, 35*).

CONCLUSION

We have proposed and tested on a set of phantom studies and demonstrated on clinical data a multimodal methodology for quantitative resolution recovery for whole body PET-CT, here specifically designed for ^{18}F-Fluoride PET imaging of bone metastases. The technique allows rapid and straightforward application and produces images of significant improved visual quality and quantitative properties.

ACKNOWLEDGMENTS

The project is supported by the EPSRC, the NIHR Biomedical Research Centre at Guy's and St Thomas' NHS Foundation Trust and King's College London and UCL

Comprehensive Cancer Imaging Centre funded by the CRUK and EPSRC in association with the MRC and DoH (England).

Elisabetta Grecchi is also supported by an EPSRC scholarship (EP/K502868/1).

Jim O'Doherty is also supported by the Centre of Excellence in Medical Engineering, Wellcome Trust and EPSRC grant number WT 088641/Z/09/Z.

Federico E Turkheimer and Mattia Veronese are supported by the MRC PET Methodology Program grant (G1100809/1).

The views expressed are those of the authors and not necessarily those of the NHS, the NIHR or the Department of Health.

We wish also to acknowledge Dr. Benjamin Taylor for providing us anonymised patient data.

DISCLOSURE

The authors have no conflict of interest to disclose, financial or otherwise.

REFERENCES

1. Rubens RD. Bone metastases: incidence and complications. In: Rubens RD, Mundy GR, eds. *Cancer and the Skeleton*. London: Martin Dunitz; 2000:33-42.

2. Coleman RE, Rubens RD. The clinical course of bone metastases from breast cancer. *British journal of cancer.* 1987;55:61.

3. Clamp A, Danson S, Nguyen H, Cole D, Clemons M. Assessment of therapeutic response in patients with metastatic bone disease. *The lancet oncology.* 2004;5:607-616.

4. Therasse P, Arbuck SG, Eisenhauer EA, et al. New guidelines to evaluate the response to treatment in solid tumors. *Journal of the National Cancer Institute.* 2000;92:205-216.

5. Scher HI, Halabi S, Tannock I, et al. Design and end points of clinical trials for patients with progressive prostate cancer and castrate levels of testosterone: recommendations of the Prostate Cancer Clinical Trials Working Group. *Journal of Clinical Oncology.* 2008;26:1148-1159.

6. Coleman RE, Mashiter G, Whitaker KB, Moss DW, Rubens RD, Fogelman I. Bone scan flare predicts successful systemic therapy for bone metastases. *J Nucl Med.* 1988;29:1354-1359.

7. Even-Sapir E, Metser U, Flusser G, et al. Assessment of malignant skeletal disease: initial experience with 18F-fluoride PET/CT and comparison between 18F-fluoride PET and 18F-fluoride PET/CT. *Journal of Nuclear Medicine.* 2004;45:272-278.

8. Even-Sapir E, Metser U, Mishani E, Lievshitz G, Lerman H, Leibovitch I. The detection of bone metastases in patients with high-risk prostate cancer: 99mTc-MDP Planar bone scintigraphy, single-and multi-field-of-view SPECT, 18F-fluoride PET, and 18F-fluoride PET/CT. *Journal of Nuclear Medicine.* 2006;47:287-297.

9. Galasko CSB. The pathological basis for skeletal scintigraphy. *Journal of Bone & Joint Surgery, British Volume.* 1975;57:353-359.

10. Ptáček J, Henzlová L, Koranda P. Bone SPECT image reconstruction using deconvolution and wavelet transformation: Development, performance assessment and comparison in phantom and patient study with standard OSEM and resolution recovery algorithm. *Physica Medica.* 2014;30:858-864.

11. Woodbury DH, Beierwaltes WH. Fluorine-18 uptake and localization in soft tissue deposits of osteogenic sarcoma in rat and man. *Journal of Nuclear Medicine.* 1967;8:646-651.

12. Beheshti M, Vali R, Waldenberger P, et al. The use of F-18 choline PET in the assessment of bone metastases in prostate cancer: correlation with morphological changes on CT. *Molecular Imaging and Biology.* 2009;11:446-454.

13. Young H, Baum R, Cremerius U, et al. Measurement of clinical and subclinical tumour response using [18 F]-fluorodeoxyglucose and positron emission tomography: review and 1999 EORTC recommendations. *European journal of cancer.* 1999;35:1773-1782.

14. Stefano A, Gallivanone F, Messa C, Gilardi MC, Gastiglioni I. Metabolic impact of partial volume correction of [18F] FDG PET-CT oncological studies on the assessment of tumor response to treatment. *The quarterly journal of nuclear medicine and molecular imaging: official publication of the Italian Association of Nuclear Medicine (AIMN)[and] the International Association of Radiopharmacology (IAR),[and] Section of the Society of.* 2014;58:413-423.

15. Hatt M, Groheux D, Martineau A, et al. Comparison between 18F-FDG PET image–derived indices for early prediction of response to neoadjuvant chemotherapy in breast cancer. *Journal of Nuclear Medicine.* 2013;54:341-349.

16. Soret M, Bacharach SL, Buvat I. Partial-volume effect in PET tumor imaging. *Journal of Nuclear Medicine.* 2007;48:932-945.

17. Rousset O, Rahmim A, Alavi A, Zaidi H. Partial volume correction strategies in PET. *PET clinics.* 2007;2:235-249.

18. Meltzer CC, Zubieta JK, Links JM, Brakeman P, Stumpf MJ, Frost JJ. MR-based correction of brain PET measurements for heterogeneous gray matter radioactivity distribution. *Journal of Cerebral Blood Flow & Metabolism.* 1996;16:650-658.

19. Boussion N, Hatt M, Lamare F, Le Rest CC, Visvikis D. Contrast enhancement in emission tomography by way of synergistic PET/CT image combination. *Computer methods and programs in biomedicine.* 2008;90:191-201.

20. Shidahara M, Tsoumpas C, Hammers A, et al. Functional and structural synergy for resolution recovery and partial volume correction in brain PET. *Neuroimage.* 2009;44:340-348.

21. Aston JAD, Cunningham VJ, Asselin M-C, Hammers A, Evans AC, Gunn RN. Positron emission tomography partial volume correction: Estimation and Algorithms. *Journal of Cerebral Blood Flow & Metabolism.* 2002;22:1019-1034.

22. Rousset OG, Ma Y, Evans AC. Correction for partial volume effects in PET: principle and validation. *Journal of Nuclear Medicine.* 1998;39:904-911.

23. Qi J, Leahy RM, Cherry SR, Chatziioannou A, Farquhar TH. High-resolution 3D Bayesian image reconstruction using the microPET small-animal scanner. *Physics in medicine and biology.* 1998;43:1001.

24. Rapisarda E, Bettinardi V, Thielemans K, Gilardi M. Image-based point spread function implementation in a fully 3D OSEM reconstruction algorithm for PET. *Physics in medicine and biology.* 2010;55:4131.

25. Alessio AM, Stearns CW, Tong S, et al. Application and evaluation of a measured spatially variant system model for PET image reconstruction. *Medical Imaging, IEEE Transactions on.* 2010;29:938-949.

26. Hammers A, Allom R, Koepp MJ, et al. Three‐dimensional maximum probability atlas of the human brain, with particular reference to the temporal lobe. *Human brain mapping.* 2003;19:224-247.

27. Turkheimer FE, Boussion N, Anderson AN, Pavese N, Piccini P, Visvikis D. PET image denoising using a synergistic multiresolution analysis of structural (MRI/CT) and functional datasets. *Journal of Nuclear Medicine.* 2008;49:657-666.

28. Molteni R. Prospects and challenges of rendering tissue density in Hounsfield units for cone beam computed tomography. *Oral surgery, oral medicine, oral pathology and oral radiology.* 2013;116:105-119.

29. Kudo H, Nomura M, Asada T, Takeda T. Image processing method for analyzing cerebral blood-flow using SPECT and MRI. Paper presented at: Nuclear Science Symposium Conference Record, 2007. NSS'07. IEEE, 2007.

30. Grecchi E, O'Doherty J, Turkheimer FE. Exploiting anatomical information for PET image enhancement: a phantom experiment for algorithm validation. Paper presented

at: Nuclear Science Symposium and Medical Imaging Conference (NSS/MIC), 2014 IEEE; Nov. 8 2014-Nov. 15 2014, 2014.

31. Hatt M, Le Pogam A, Visvikis D, Pradier O, Le Rest CC. Impact of partial-volume effect correction on the predictive and prognostic value of baseline 18F-FDG PET images in esophageal cancer. *Journal of Nuclear Medicine.* 2012;53:12-20.

32. Hoetjes NJ, van Velden FHP, Hoekstra OS, et al. Partial volume correction strategies for quantitative FDG PET in oncology. *European journal of nuclear medicine and molecular imaging.* 2010;37:1679-1687.

33. Thielemans K, Asma E, Ahn S, et al. Impact of PSF modelling on the convergence rate and edge behaviour of EM images in PET. Paper presented at: Nuclear Science Symposium Conference Record (NSS/MIC), 2010 IEEE, 2010.

34. Cook GJ, Yip C, Siddique M, et al. Are pretreatment 18F-FDG PET tumor texturalfFeatures in non–small cell lung cancer associated with response and survival after chemoradiotherapy? *Journal of Nuclear Medicine.* 2013;54:19-26.

35. Hatt M, Majdoub M, Vallieres M, et al. 18F-FDG PET uptake characterization through texture analysis: investigating the complementary nature of heterogeneity and functional tumor volume in a multi–cancer site patient cohort. *Journal of Nuclear Medicine.* 2015;56:38-44.

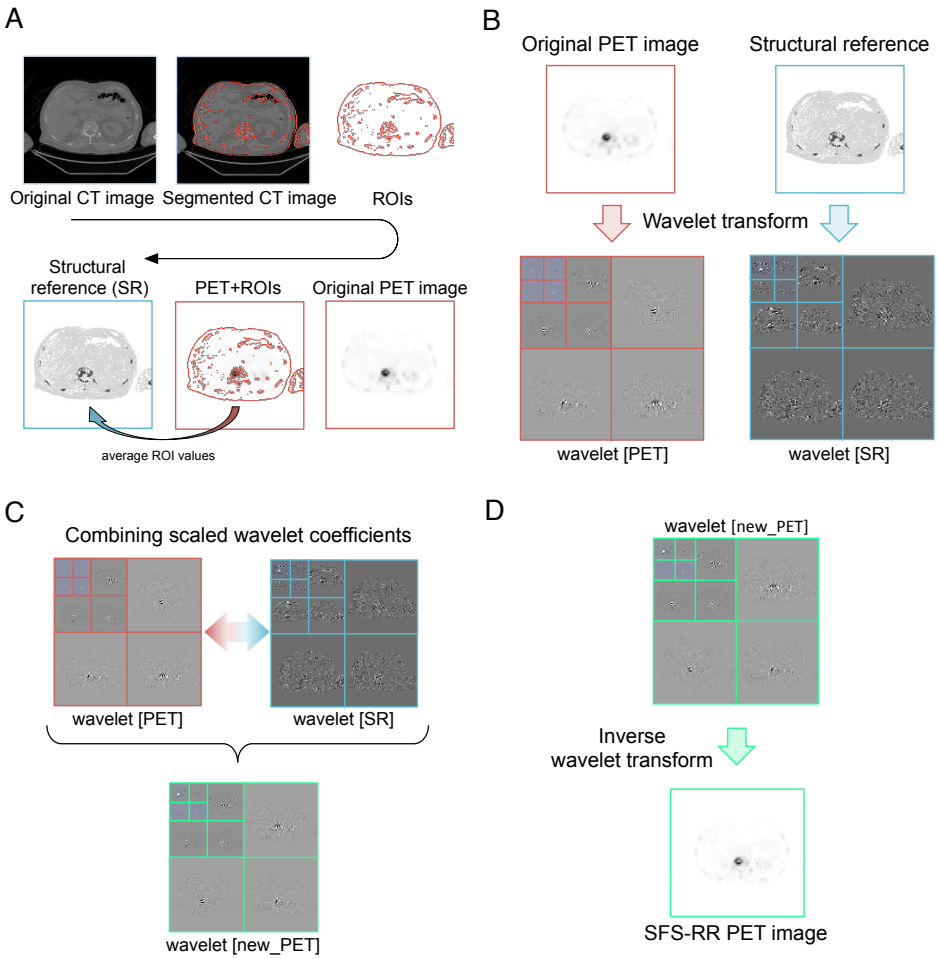

Figure 1 Graphical representation of the SFS-RR algorithm. A) The structural reference image required by the SFS-RR algorithm is computed from the CT and PET images; B) wavelet decomposition of functional and structural images; C) the functional and structural wavelet coefficients are combined to get the new high-resolution PET coefficients; D) inverse wavelet transform of the coefficients obtained from step C resulting in the new high-resolution SFS-RR PET image. For a detailed mathematical formulation refer to the Supplementary Materials.

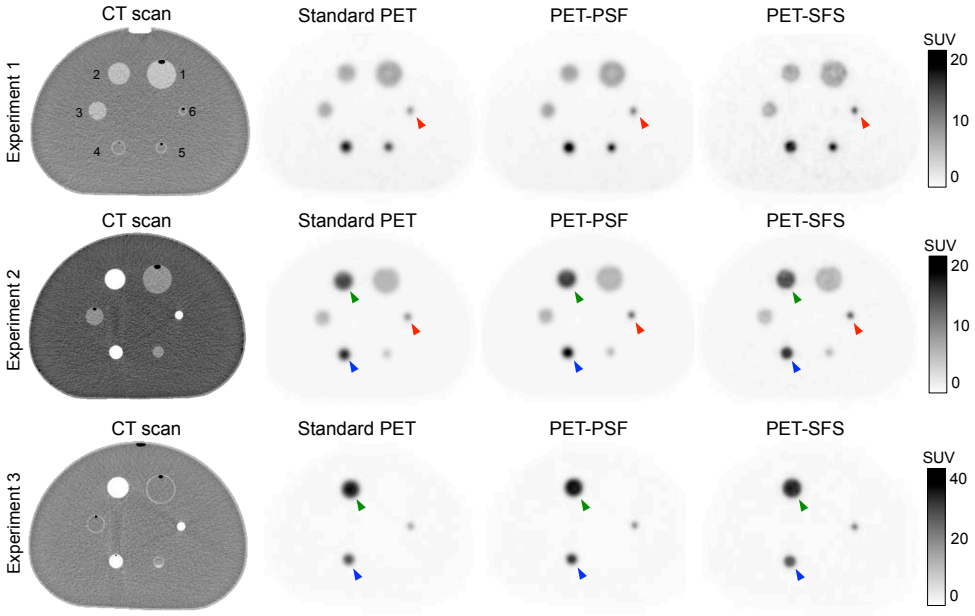

Figure 2 [^{18}F]Fluoride PET-CT transaxial images of three different phantom experiment acquisitions (one for each line). Alongside the CT image (1st column) are three different type of functional images: standard PET images (2nd column), images resulting from the inclusion of a PSF model into the reconstruction (3rd column) and images resulting after the application of the SFS resolution recovery algorithm (4th column).

For detailed information on lesions volume, CM and 18F-FDG concentrations we refer to Table 1.

Green markers highlight sphere 2, blue markers highlight sphere 4 and red markers highlight sphere 6.

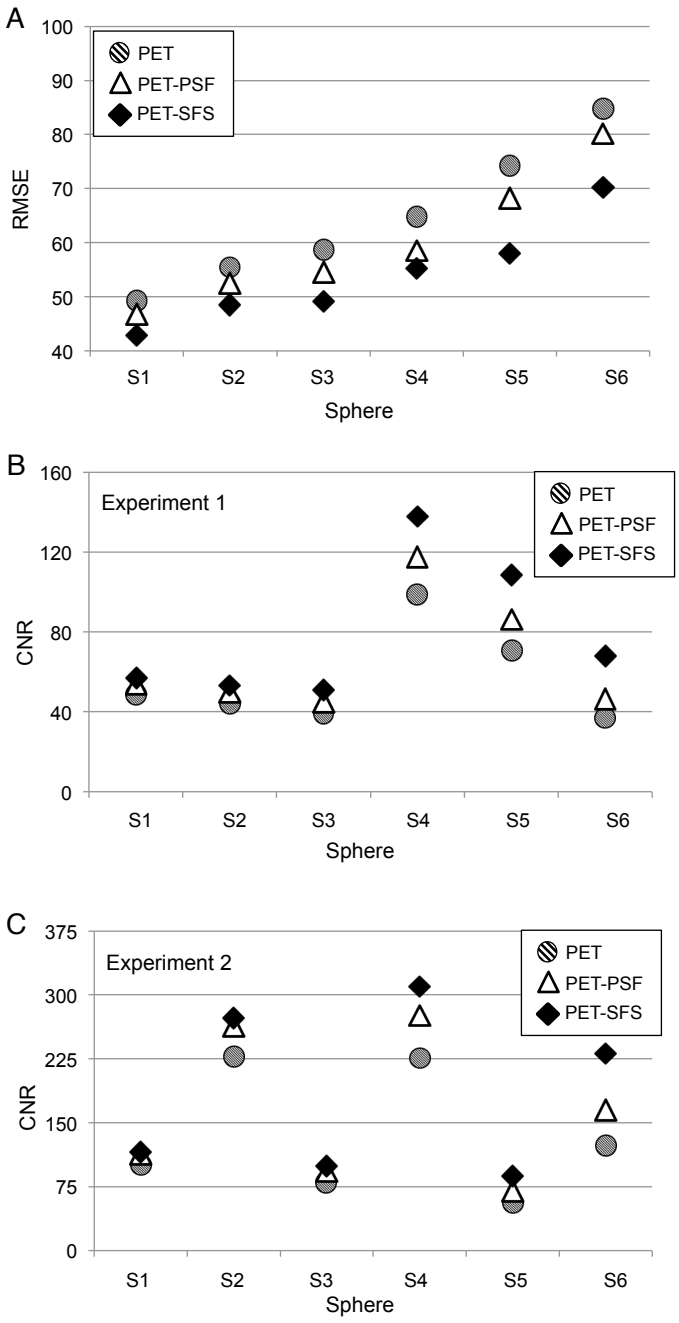

Figure 3 Root mean square error and noise analysis. For each sphere (S1-S6) three values corresponding to images obtained with different modalities are reported: standard PET (dashed circle), PET with PSF reconstruction (white triangle) and PET corrected with SFS-RR algorithm (black diamond)

A) Root mean square error for the six spheres obtained as an average among the three phantom experiments. B-C) Contrast to noise ratio computed for each sphere against a uniform region in the phantom background. Only experiments 1 and 2 are reported for consistency reasons (in experiment 3 three spheres have zero activity).

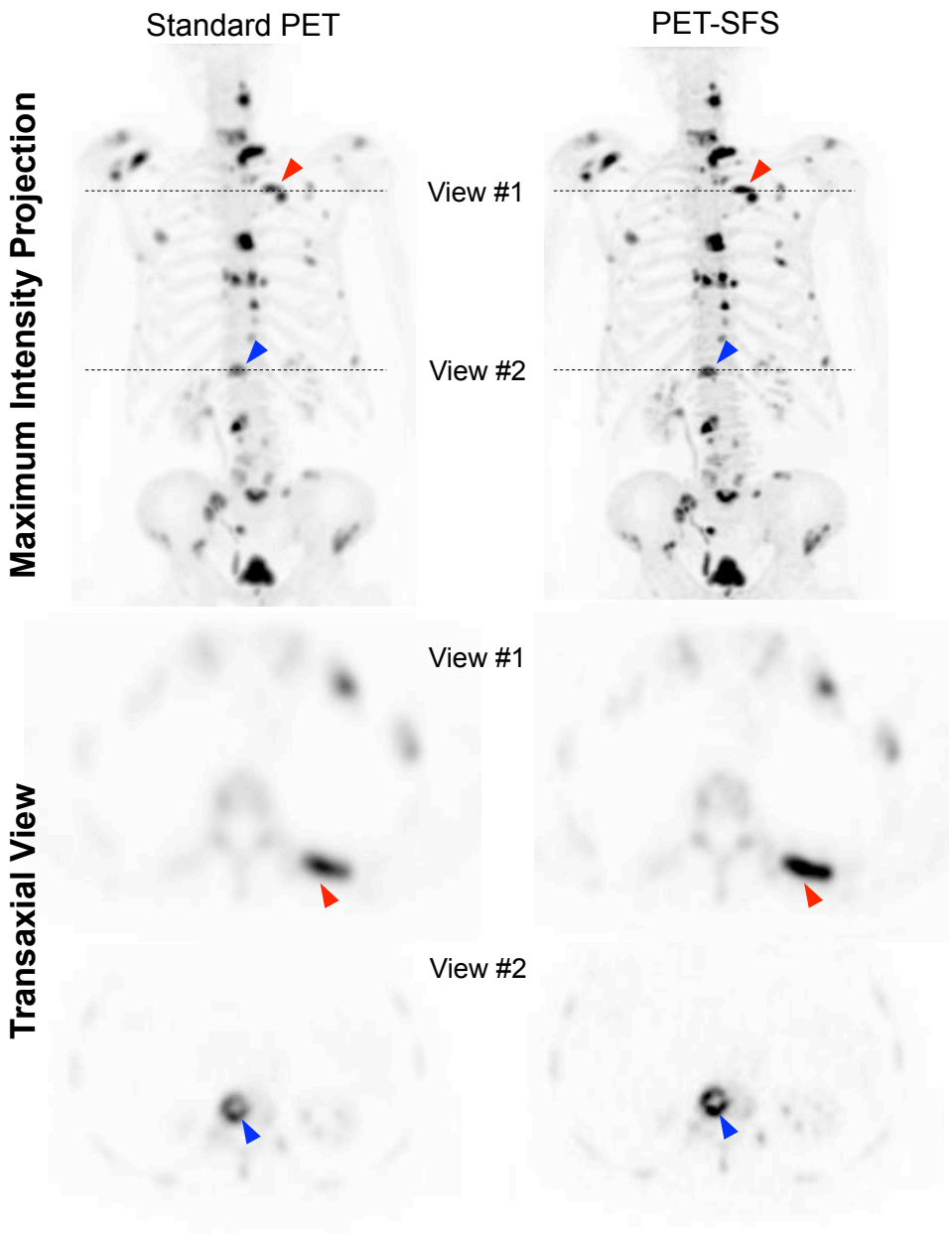

Figure 4 Maximum Intensity Projection (MIP) and transaxial views of a representative subject (Patient 01). Left Panel - Standard PET; Right Panel - PET corrected with SFS-RR algorithm. The red and blue markers highlight two representative lesions (spine and rib respectively) that appear sharper in the PET-SFS image compared to the standard PET one. Dashed lines indicate the slice position of the transaxial views reported below the MIP.

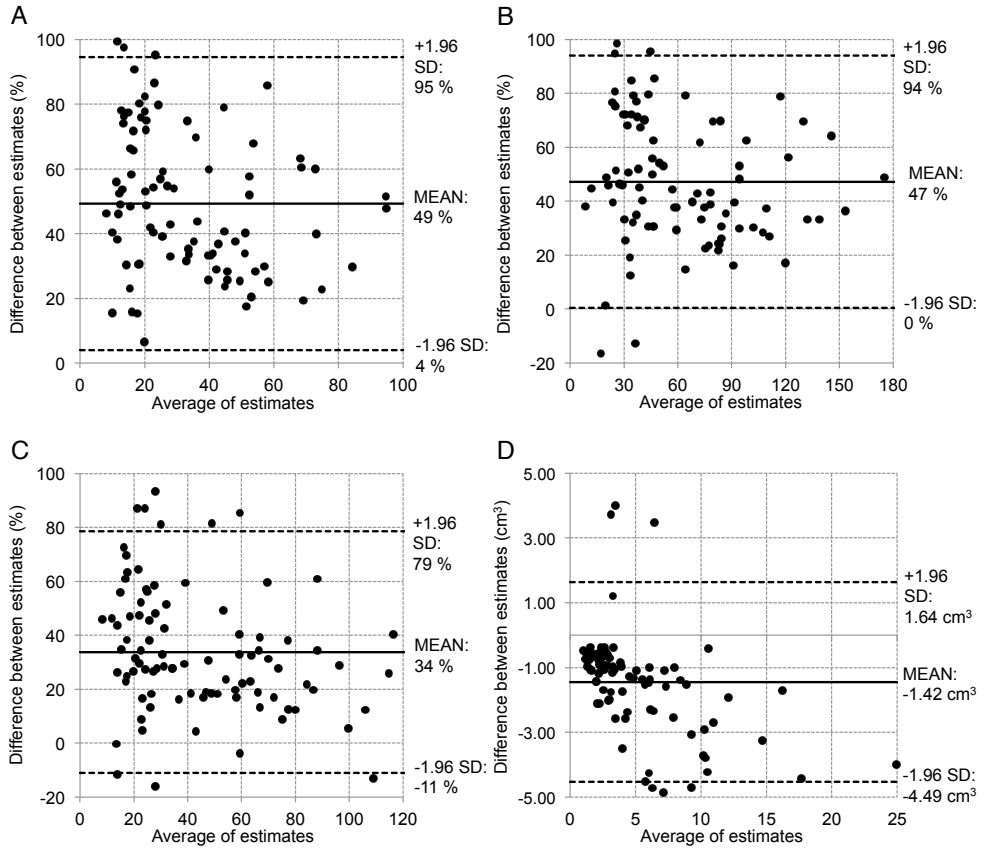

Figure 5 Bland-Altman plots showing the differences in MATV and activity quantification when estimates are computed in images obtained with standard PET and PET corrected with the SFS-RR algorithm. Each grey circle represents a specific lesion; all lesions of all patients are reported. The differences between estimates for SUV_{mean} (A), SUV_{max} (B) and SUV_{peak} (C) are reported as the relative percentage difference. The MATV (D) is reported as absolute difference in cm^3.

TABLES

Table 1

CT CONTRAST MEDIA AND PET RADIOTRACER CONCENTRATIONS

Phantom	Experiment 1		Experiment 2		Experiment 3		
Compartments	Iodine CM [mg/ml]	^{18}F-FDG [kBq/ml]	Iodine CM [mg/ml]	^{18}F-FDG [kBq/ml]	Iodine CM [mg/ml]	^{18}F-FDG [kBq/ml]	Sphere Volume [ml]
Background	1.08 *	4.56 *	1.20 *	5.29 *	1.20 *	5.70 *	9700
S1	6.00 †	53.20 †	6.00 †	66.50 †	1.20 *	5.70 *	26.52
S2	6.00 †	53.20 †	42.00 ‡	187.00 ‡	41.20 ‡	227.00 ‡	11.49
S3	6.00 †	53.20 †	6.00 †	66.50 †	1.20 *	5.70 *	5.57
S4	1.00 *	148.50 ‡	42.00 ‡	187.00 ‡	41.20 ‡	227.00 ‡	2.57
S5	1.00 *	148.50 ‡	6.00 †	66.50 †	1.20 *	5.70 *	1.15
S6	1.00 *	148.50 ‡	42.00 ‡	187.00 ‡	41.20 ‡	227.00 ‡	0.52

Concentrations of Iodine (from Omnipaque300^{TM}) and ^{18}F-FDG injected in all phantom compartments for each experiment. Compartments volumes are also reported.

To note that spheres 4-6 Experiment 1 and spheres 1,3,5 Experiment 3 are filled with the same radioactivity concentration as the background – as a result they are indiscernible in the PET image.

* Concentration resulting in image contrast comparable to normal soft tissue

† Concentration resulting in image contrast comparable to normal bone

‡ Concentration resulting in image contrast comparable to metastatic bone